

## R2D2: Deep neural network series for near real-time high-dynamic range imaging in radio astronomy

AMIR AGHABIGLOU ,<sup>1</sup> CHUNG SAN CHU ,<sup>1</sup> ADRIAN JACKSON ,<sup>2</sup> ARWA DABBECH ,<sup>1</sup> AND YVES WIAUX ,<sup>1</sup>

<sup>1</sup>*Institute of Sensors, Signals and Systems, Heriot-Watt University, Edinburgh EH14 4AS, United Kingdom*

<sup>2</sup>*EPCC, University of Edinburgh, Edinburgh EH8 9BT, United Kingdom*

### ABSTRACT

We present a novel AI approach for high-resolution high-dynamic range synthesis imaging by radio interferometry (RI) in astronomy. R2D2, standing for “**R**esidual-to-**R**esidual **D**NN series for high-**D**ynamic range imaging”, is a model-based data-driven approach relying on hybrid deep neural networks (DNNs) and data-consistency updates. Its reconstruction is built as a series of residual images estimated as the outputs of DNNs, each taking the residual dirty image of the previous iteration as an input. The approach can be interpreted as a learned version of a matching pursuit approach, whereby model components are iteratively identified from residual dirty images, and of which CLEAN is a well-known example. We propose two variants of the R2D2 model, built upon two distinctive DNN architectures: a standard U-Net, and a novel unrolled architecture. We demonstrate their use for monochromatic intensity imaging on highly-sensitive observations of the radio galaxy Cygnus A at S band, from the Very Large Array (VLA). R2D2 is validated against CLEAN and the recent RI algorithms AIRI and uSARA, which respectively inject a learned implicit regularization and an advanced handcrafted sparsity-based regularization into the RI data. With only few terms in its series, the R2D2 model is able to deliver high-precision imaging, significantly superior to CLEAN and matching the precision of AIRI and uSARA. In terms of computational efficiency, R2D2 runs at a fraction of the cost of AIRI and uSARA, and is also faster than CLEAN, opening the door to real-time precision imaging in RI.

*Keywords:* Astronomy image processing (2306) — Computational methods (1965) — Neural networks (1933) — Aperture synthesis (53) — Radio galaxies (1343)

### 1. INTRODUCTION

Modern radio telescopes are able to map the radio sky over large fields of view and wide frequency bandwidths with great depth and detail, owing to the sheer amounts of the data they acquire. Leveraging these capabilities in image formation raises significant data-processing challenges. The underlying RI inverse problem calls for efficient imaging algorithms able to deliver high-precision reconstruction via tailored regularization models, while scaling to the large data volumes and targeted image dimensions. Over the past two decades, numerous imaging algorithms for RI emerged from optimization theory (e.g., Wiaux et al. 2009; Li et al. 2011; Carrillo et al. 2012; Garsden et al. 2015; Dabbech et al. 2015; Repetti

& Wiaux 2020). Backed by compressive sensing theory, these algorithms are propelled by advanced hand-crafted sparsity-based image models injected to the RI data, and underpinned by convergent algorithmic structures stemming from optimization theory. However, the complexity and highly-iterative nature of the underlying algorithmic structures have hindered their adoption by the wider radio astronomy community. Since its inception by Högbom (1974), the CLEAN algorithm remains the standard technique for RI imaging owing to its simplicity and relatively low computational cost. Variants of CLEAN have been devised over five decades to overcome its shortfalls in terms of precision and stability (e.g., Wakker & Schwarz 1988; Bhatnagar & Cornwell 2004; Cornwell 2008). Nonetheless, CLEAN reconstruction is by design limited in resolution and sensitivity.

Very recently, novel algorithms for computational imaging empowered by deep learning (DL) have emerged across a wide range of applications, including RI. While

Corresponding author: Yves Wiaux  
 y.wiaux@hw.ac.uk

purely data-driven end-to-end DNNs can provide real-time solutions to the RI inverse problem (Connor et al. 2022; Schmidt, K. et al. 2022), they raise important interpretability and reliability concerns as standard architectures cannot ensure consistency of the recovered image with the observed data. Additionally, they are yet to be validated in large-scale high-sensitivity high-resolution data acquisition regimes. Alternative Plug-and-Play (PnP) approaches, interfacing optimization theory and DL, can circumvent these concerns by implicitly injecting a learned image model into the data, via pre-trained denoising DNNs (see Kamilov et al. 2023, for a review). Among such methods, AIRI (“AI for Regularization in radio-interferometric Imaging”, Terris et al. 2022) has demonstrated state-of-the-art precision imaging when validated on real large-scale observations from modern radio telescopes (Dabbech et al. 2022; Wilber et al. 2023b). Nonetheless, PnP approaches remain highly iterative, which undermines their scalability to the extreme data and image dimensions expected from next-generation radio telescopes such as the upcoming Square Kilometre Array<sup>1</sup>, and ultimately, their adoption.

Since their inception as fast approximations for sparse coding (Gregor & LeCun 2010), unrolled (or unfolded) DNNs have gained enormous attention by the computational imaging community (see Monga et al. 2021, for a review). Conceptually, they can inherit domain knowledge (for example, the measurement operator to ensure data consistency) and prior models by unfolding the iterations of an iterative algorithm as layers of the network architecture. Therefore, unrolled DNNs tend to offer more interpretability and generalizability than purely data-driven DNNs. Yet, these model-based DL methods can be overly expensive for extreme sampling modalities. In fact, embedding large-scale (RI) measurement operators in the network architecture is impractical for both the training stage and the inference stage (i.e., when applying them for image reconstruction).

In this article, we propose a novel DL approach dubbed R2D2, standing for **R**esidual-to-**R**esidual **D**NN series for high-**D**ynamic range imaging. Reminiscent of a matching pursuit algorithm, R2D2 circumvents the issue of embedding large-scale measurement operators into DNNs by effectively externalizing data consistency operations from the network architecture. We propose two variants of R2D2, built upon two distinct DNN architectures; the first adopting a standard U-Net architecture, and the second leveraging a novel unrolled

DNN architecture inspired by the R2D2 model itself. We demonstrate the R2D2 model through its two variants on highly-sensitive VLA observations of the radio galaxy Cygnus A at S band. We showcase that only a few iterations are required to achieve a near real-time reconstruction, with R2D2 superseding the most advanced multiscale variant of CLEAN (Offringa et al. 2014) in both computational time and reconstruction quality, and offering a precision that is on par with the recently proposed algorithms uSARA and AIRI (Repetti & Wiaux 2020; Terris et al. 2022).

The remainder of this paper is structured as follows. Section 2 provides a summary of the RI inverse problem. Section 3 elaborates on the R2D2 model, from its intrinsic concept to its two proposed variants and their underlying network architectures. Section 4 provides the training details of VLA-specific R2D2 models. Validation of these VLA-specific incarnations on Cygnus A observations against the benchmark methods for RI is presented in Section 5. Conclusions and future research are summarized in Section 6.

## 2. RI IMAGING INVERSE PROBLEM

Under the assumptions of monochromatic, non-polarized radio emission spanning a narrow field of view, RI data are noisy Fourier measurements of the sought radio image. The sampled Fourier coverage is defined by the array antenna configuration and the specifications of the observation (e.g., direction of sight, total observation time, integration time). Consider  $\mathbf{x}^* \in \mathbb{R}_+^N$  a discrete representation of the unknown radio image. A discrete model of the RI data, denoted by the vector  $\mathbf{y} \in \mathbb{C}^M$ , reads  $\mathbf{y} = \Phi \mathbf{x}^* + \mathbf{n}$ , where  $\mathbf{n} \in \mathbb{C}^M$  is a realization of an additive white Gaussian noise, with zero-mean and a standard deviation  $\tau > 0$ . The RI measurement operator  $\Phi \in \mathbb{C}^{M \times N}$  is a Fourier sampling operator, often involving a data-weighting scheme to mitigate the non-uniform Fourier sampling and enhance the effective resolution of the data (e.g. Briggs weighting; Briggs 1995). In high-sensitivity data acquisition regimes, the measurement operator model can be more complex, encompassing direction dependent effects of different origins, from geometric phase delays to atmospheric perturbations or instrument errors (Smirnov 2011). The RI inverse problem is ill-posed due to the incompleteness of the Fourier sampling and the measurement noise.

The image-domain expression of the RI inverse problem can be achieved by back-projecting the data  $\mathbf{y}$  via the adjoint of the measurement operator as follows:

$$\mathbf{x}_d = \mathbf{D} \mathbf{x}^* + \mathbf{b}, \quad (1)$$

where  $\mathbf{x}_d = \kappa \text{Re}\{\Phi^\dagger \mathbf{y}\} \in \mathbb{R}^N$  is the normalized back-projected data, often referred to as the *dirty* image,

<sup>1</sup> [www.skao.int/](http://www.skao.int/)

with  $(\cdot)^\dagger$  denoting the adjoint of its argument operator. The normalization factor  $\kappa > 0$  ensures that the point spread function (PSF,  $\mathbf{h} = \kappa \operatorname{Re}\{\Phi^\dagger \Phi\} \boldsymbol{\delta} \in \mathbb{R}^N$ , with  $\boldsymbol{\delta} \in \mathbb{R}^N$  standing for the image with value one at its center and zero otherwise) has a peak value equal to one. The linear operator  $\mathbf{D} \in \mathbb{R}^{N \times N}$ , mapping the image of interest to the dirty image space, is defined as  $\mathbf{D} \triangleq \kappa \operatorname{Re}\{\Phi^\dagger \Phi\}$ , encoding Fourier de-gridding and gridding operations. Finally, the image-domain noise vector  $\mathbf{b} = \kappa \operatorname{Re}\{\Phi^\dagger \mathbf{n}\} \in \mathbb{R}^N$  stands for the normalized back-projected noise.

### 3. METHODS

#### 3.1. R2D2 model

The R2D2 model is underpinned by a sequence of DNNs denoted by  $(\mathbf{N}_{\widehat{\boldsymbol{\theta}}^{(i)}})_{1 \leq i \leq I}$ , which are described by their learned parameters  $(\widehat{\boldsymbol{\theta}}^{(i)} \in \mathbb{R}^Q)_{1 \leq i \leq I}$ . The image estimate is initialized as  $\mathbf{x}^{(0)} = \mathbf{0} \in \mathbb{R}^N$ . At a given iteration  $i \in \{1, \dots, I\}$ , the network  $\mathbf{N}_{\widehat{\boldsymbol{\theta}}^{(i)}}$  takes as input the residual dirty image, updated from the dirty image by removing the contribution of the previous image estimate as follows:

$$\mathbf{r}^{(i-1)} = \mathbf{x}_d - \mathbf{D}\mathbf{x}^{(i-1)}. \quad (2)$$

The output of the network is then used to update the image estimate as:

$$\mathbf{x}^{(i)} = \mathbf{x}^{(i-1)} + \mathbf{N}_{\widehat{\boldsymbol{\theta}}^{(i)}}(\mathbf{r}^{(i-1)}). \quad (3)$$

The predicted residual image  $\mathbf{N}_{\widehat{\boldsymbol{\theta}}^{(i)}}(\mathbf{r}^{(i-1)})$  captures emission from the input residual dirty image  $\mathbf{r}^{(i-1)}$ , and corrects for estimation errors in  $\mathbf{x}^{(i-1)}$ , progressively enhancing the resolution and dynamic range of the reconstruction. Assuming  $I$  networks in the R2D2 sequence, the final reconstruction  $\widehat{\mathbf{x}}$  takes the simple series expression below:

$$\widehat{\mathbf{x}} \triangleq \mathbf{x}^{(I)} = \sum_{i=1}^I \mathbf{N}_{\widehat{\boldsymbol{\theta}}^{(i)}}(\mathbf{r}^{(i-1)}). \quad (4)$$

In principle, the number of networks in the series should be devised to ensure that the residual dirty image corresponds to noise. Interestingly, extensive tests on RI simulations (subject of an upcoming paper) suggest that only a small number of terms in the series is necessary to reach the expected image-domain noise levels, achieving high-dynamic range images with noise-compatible residual dirty images. This is also observed on real data results (see Section 5).

An illustration of the R2D2 model is provided in Fig. 1. Intuitively, it can be interpreted as a learned version of the matching pursuit algorithm, iteratively

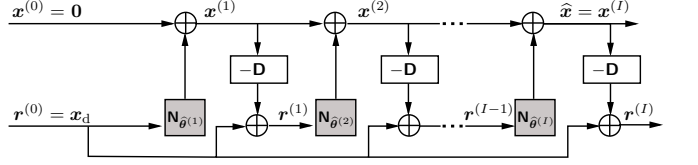


**Figure 1.** Illustration of the R2D2 model. The top and bottom rows respectively show the update of the image estimates  $(\mathbf{x}^{(i)})_{1 \leq i \leq I}$  and the residual dirty images  $(\mathbf{r}^{(i-1)})_{1 \leq i \leq I}$ , i.e., normalized back-projected data residuals. The latter are fed to the networks  $(\mathbf{N}_{\widehat{\boldsymbol{\theta}}^{(i)}})_{1 \leq i \leq I}$  and the former are updated from the networks' output, i.e., the predicted residual images.

identifying model components from back-projected data residuals. On the one hand, our proposed model-based DL approach combines elements of PnP algorithms based on the Forward-Backward optimization algorithm. On the other hand, it distinguishes itself from traditional unrolled architectures through a novel sequential training procedure, with the often computationally-demanding mapping operator  $\mathbf{D}$  being fully externalized from the networks and their typical GPU implementation. This unique approach enables enforcing data fidelity through accurate models of the measurement operator both during training and inference. In fact, where appropriate, distributed implementations of the measurement operator can easily be leveraged to scale up to large data sizes (Dabbech et al. 2022), typically implemented on flexible CPU-based high-performance computing (HPC) systems.

#### 3.2. R2D2 training losses

Consider the training dataset composed of the ground truth images  $(\mathbf{x}_k^*)_{1 \leq k \leq K}$ , and their associated dirty images  $(\mathbf{r}_k^{(0)} = \mathbf{x}_{d_k})_{1 \leq k \leq K}$ . Initializing  $(\mathbf{x}_k^{(0)} = \mathbf{0})_{1 \leq k \leq K}$ , for each iteration  $i \in \{1, \dots, I\}$ , the associated network is trained, taking the previous residual dirty images  $(\mathbf{r}_k^{(i-1)})_{1 \leq k \leq K}$  as input, and invoking the image pairs  $(\mathbf{x}_k^*, \mathbf{x}^{(i-1)})_{1 \leq k \leq K}$  in its loss function. More precisely, the trained  $\mathbf{N}_{\widehat{\boldsymbol{\theta}}^{(i)}}$  is described by its learned parameter vector  $\widehat{\boldsymbol{\theta}}^{(i)}$ , the minimizer of the loss function:

$$\min_{\boldsymbol{\theta}^{(i)} \in \mathbb{R}^Q} \frac{1}{K} \sum_{k=1}^K \|\mathbf{x}_k^* - [\mathbf{x}_k^{(i-1)} + \mathbf{N}_{\boldsymbol{\theta}^{(i)}}(\mathbf{r}_k^{(i-1)})]_+\|_1, \quad (5)$$

where  $\|\cdot\|_1$  stands for the  $\ell_1$ -norm, and  $[\cdot]_+$  denotes the projection onto the positive orthant  $\mathbb{R}_+^N$ , ensuring the non-negativity of the image estimate at any point in the iterative sequence. From the estimated model images, the residual dirty images  $(\mathbf{r}_k^{(i)})_{1 \leq k \leq K}$  are updated as described by (2). Then, they are fed to the subsequent DNN for training. As highlighted in Section 3.1, the sequential building of the R2D2 model relies on hybrid

computational resources; CPU resources for the computations of the residual dirty images, and GPU resources for the training of its underlying DNNs, as well as their application at inference stage.

### 3.3. R2D2 network architectures

We introduce two variants of the R2D2 model, each employing a distinctive architecture underlying their network components  $(\mathbf{N}_{\hat{\theta}^{(i)}})_{1 \leq i \leq I}$ .

**U-Net**—The first variant, simply referred to as R2D2 henceforth, relies on the widely-used U-Net architecture (Ronneberger et al. 2015). Let  $\beta \in \mathbb{R}^P$  denote the vector representation of its parameters. The U-Nets of R2D2 are trained sequentially using the losses (5). For each iteration  $i \in \{1, \dots, I\}$ , the learned parameters of the  $i^{\text{th}}$  U-Net in R2D2 correspond to  $\hat{\theta}^{(i)} = \beta^{(i)} \in \mathbb{R}^P$ , with  $Q = P$ .

**R2D2-Net**—The second variant introduces a novel, and more complex architecture, dubbed R2D2-Net, substituting the U-Net as the core network of the R2D2 sequence. R2D2-Net consists of  $J$  U-Net blocks interlaced with  $J - 1$  approximate data consistency layers. Its learned parameters read  $[\beta^{(1)}, \dots, \beta^{(J)}] \in \mathbb{R}^{P \times J}$ . The data consistency layers of R2D2-Net call for convolutions with the PSF (see expression in Section 2) when mapping the image estimate to the dirty image space. This mapping is a fast and memory-efficient approximation of the fully accurate operator  $\mathbf{D}$ , making the *approximate* consistency to the data integral to the training of R2D2-Net. In essence, R2D2-Net is an unrolled variant of the R2D2 model, trained end-to-end, and entirely on a GPU. In fact, when injected into the R2D2 sequence, the first R2D2-Net can be depicted via the diagram of Fig. 1, with its U-Net blocks trained jointly, and considering the convolution with the PSF as the mapping operator  $\mathbf{D}$ . Subsequent R2D2-Nets in the sequence take as input the residual dirty images  $r^{(i-1)}$  as per (2). In reference to its nesting structure, we dub this variant of the R2D2 model as “**Russian Doll R2D2**”, or in short R3D3. R3D3 can be interpreted as a learned version of the Cotton-Schwab CLEAN algorithm (Schwab 1984), with R2D2-Net, its core network, being reminiscent of the CLEAN minor cycle. R3D3 harnesses (i) the efficiency of the R2D2-Net’s unrolled structure, encompassing approximate knowledge of the observation setting during training, and (ii) the robustness and scalability of its series structure, calling for accurate models of the RI measurement operator at few instances only, and on flexible computing hardware. For each iteration  $i \in \{1, \dots, I\}$ , the  $i^{\text{th}}$  R2D2-Net of R3D3 is trained us-

ing the loss (5). Its learned parameters correspond to  $\hat{\theta}^{(i)} = [\beta^{(i,1)}, \dots, \beta^{(i,J)}] \in \mathbb{R}^{P \times J}$ , with  $Q = P \times J$ .

## 4. VLA-SPECIFIC TRAINING

**Dataset**—We trained both R2D2 and R3D3 on a dataset of  $K = 19600$  pairs of images of size  $N = 512 \times 512$ , composed of curated ground truth images and their associated dirty images. Firstly, the synthetic ground truth images  $(\mathbf{x}_k^*)_{1 \leq k \leq K}$  were generated from a low-dynamic range database consisting of compressed *optical* astronomical images and medical images, to which denoising and exponentiation procedures were applied, aiming to endow them with the range of dynamic ranges of interest in RI (Terris et al. 2022). Secondly, targeting a versatile yet telescope-specific model, each of the  $K$  dirty images  $(\mathbf{x}_d)_{1 \leq k \leq K}$  was created from a different VLA sampling pattern produced by the MeqTrees software (Noordam & Smirnov 2010). The sampling patterns were generated through random variations of the observation setting (randomized time and direction of the observation, flagging, number of combined channels during imaging), resulting in a varying total number of points in the range  $[0.2, 2] \times 10^6$ . The simulated RI data were corrupted with adaptive noise levels depending on the dynamic range<sup>2</sup> of the associated ground truth image. In order to contain the number of varying parameters in this first implementation, a fixed weighting scheme was applied to all RI data, which is Briggs weighting with Briggs parameter 0. A fixed super-resolution factor of about 1.5 was also used to create the associated dirty images<sup>3</sup>, obtained via back-projection of the RI data.

**Training details**—The sequential building of R2D2 and R3D3 was conducted on Cirrus<sup>4</sup>, an HPC system, comprising CPU and GPU compute nodes. The CPU nodes on Cirrus consist of two Intel 18-core Xeon E5-2695 processors, with 256GB of memory. Its GPU nodes contain two 20-core Intel Xeon Gold 6148 processors with four NVIDIA Tesla V100-SXM2-16GB GPUs and 384GB of DRAM memory. For R2D2, its sequence was built with  $I = 5$  U-Nets, consisting of  $Q = 31 \times 10^6$  parameters, each. The U-Nets were trained with the losses (5), solved with the Root Mean Squared Propagation (RMSprop) optimizer and a learning rate of  $10^{-4}$  each, and a combined number of epochs of 750. The full pro-

<sup>2</sup> The dynamic range of the ground truth image is defined as the ratio between the peak and the lowest non-zero pixel values.

<sup>3</sup> The super-resolution factor is the ratio between the imaged spatial bandwidth and the instrumental spatial bandwidth, often set in the range [1.5, 2.5].

<sup>4</sup> [www.cirrus.ac.uk](http://www.cirrus.ac.uk)

cess utilized 300 GPU hours for the training and 8064 CPU hours for the computations of the residual dirty images. As for R3D3, it was built with  $I = 4$  R2D2-Nets, each consisting of  $J = 6$  U-Net blocks and a total number of parameters  $Q = 186 \times 10^6$ . R2D2-Nets were trained with the losses (5), also solved with RMSprop and a learning rate of  $10^{-4}$  each, and a combined epoch count of 173. The full process utilized 484 GPU hours for the training and 5951 CPU hours for the computations of the residual dirty images. The number of terms in R2D2 and R3D3 was inferred from extensive testing on RI simulations. The full details of the training and the in-depth analysis of the performance of both R2D2 and R3D3 on extensive RI simulations will be covered in an upcoming paper.

## 5. VALIDATION ON CYGNUS A

Both R2D2 and R3D3 are showcased on high-sensitivity RI observations of the radio galaxy Cygnus A from the VLA. The data acquired at S band, are about 20 Megabytes in size. Careful calibration of the direction independent effects was performed in AIPS (Sebokolodi et al. 2020). The performance of R2D2 and R3D3 is studied in comparison with the state-of-the-art methods for RI: (i) AIRI (Terris et al. 2022), (ii) uSARA (Repetti & Wiaux 2020; Terris et al. 2022), and (iii) the multi-scale variant of CLEAN in the widely-used WSClean software (Offringa et al. 2014). All algorithms were run for the formation of an image of size  $N = 512 \times 512$ , with a pixel-size of 0.29 arcsec (corresponding to a super-resolution factor of 1.5), from the Briggs-weighted data (Briggs parameter set to 0). These settings are consistent with the training of R2D2 and R3D3.

The target dynamic range of Cygnus A reconstruction can be inferred from the data as the ratio between the peak pixel value of the sought image and the image-domain noise level. The latter can be estimated as  $\tau/\sqrt{2L}$ , with  $L$  denoting the spectral norm of the measurement operator (Terris et al. 2022). Under this consideration, the target dynamic range estimate is of the order  $\sim 1.7 \times 10^5$ .

### 5.1. Imaging results

Cygnus A images obtained by the different imaging algorithms are displayed in  $\log_{10}$  scale in Figs. 2–5. The images are overlaid with two additional panels: (a) a zoom on the East hotspots in  $\log_{10}$  scale, for in-depth examination of the recovered structure, and (b) the associated residual dirty image in linear scale to assess fidelity to the back-projected data. We also provide the results of the end-to-end DNNs U-Net and R2D2-Net,

**Table 1.** Numerical results of the different imaging algorithms. In assessing the computational cost, are reported the number of iterations  $n_{\text{itr}}$ , the computational time  $t_{\text{sec}}$  in seconds, and the numbers of allocated CPU cores  $n_{\text{cpu}}$  and GPUs  $n_{\text{gpu}}$  (when applicable). Data fidelity is evaluated numerically using the standard deviation of the final residual dirty image  $\sigma_{\text{residual}}$ .

	$n_{\text{itr}}$	$t_{\text{sec}}$	$n_{\text{cpu}}$	$n_{\text{gpu}}$	$\sigma_{\text{residual}}$
U-Net	1	1	-	1	0.0389
R2D2	5	10	1	1	0.0017
R2D2-Net	1	2	-	1	0.0019
R3D3	4	9	1	1	0.0009
AIRI	1977	2582	1	1	0.0007
uSARA	486	1465	1	-	0.0007
CLEAN*	8	51	1	-	0.0005

\* Number of “major cycles”.

corresponding to the first terms of the R2D2 and R3D3 series, respectively. Numerical results supporting the analysis of the reconstruction quality and the computational efficiency are provided in Table 1.

The visual inspection of the different reconstructions suggests that R3D3 (Fig. 3, top) and AIRI (Fig. 4, top) provide the best reconstructions (Fig. 4, top). uSARA (Fig. 4, bottom) presents wavelet-like artifacts, particularly visible at the inner core of Cygnus A. CLEAN (Fig. 5), on the other hand, offers the smoothest reconstruction among the iterative algorithms. Importantly, both R2D2 and R3D3 (Figs. 2–3, top) achieve highly comparable reconstruction quality to AIRI and uSARA, in general. The four algorithms provide *deep* reconstructions, whose pixel values span five orders of magnitude, that is in line with the target dynamic range estimate. Interestingly, a closer examination of the zoomed-in images of the East hotspots (panels (a) in all figures) suggests that R3D3 depicts a more physical structure at the vicinity of the hotspots (Fig. 2, top), through continuous emission, whereas AIRI, uSARA, and R2D2 (although to a lesser extent) introduce artificial zero-valued pixels at the same location. Subtle differences between R2D2 and R3D3 can be observed when examining faint extended emission. More specifically, R3D3 recovers more structure at the tails of both lobes, delivering higher dynamic range than R2D2.

Upon examination of the end-to-end trained DNNs, U-Net (Fig. 2, bottom) and R2D2-Net (Fig. 3, bottom), one can confirm the effectiveness of the series structure of the R2D2 model in enhancing both resolution and dynamic range of the final reconstructions. Firstly, U-

Net, the first iteration of R2D2, yields a coarse, highly sub-optimal representation of the radio galaxy. In contrast, R2D2-Net, the first iteration of R3D3, succeeds remarkably in forming a very good reconstruction of Cygnus A despite its inherently approximate data consistency layers. However, its sub-optimality becomes evident in its limited dynamic range when compared to the reconstruction produced by R3D3.

Both the visual examination of the residual dirty images and their corresponding standard deviation values  $\sigma_{\text{residual}}$ , reported in Table 1, indicate comparable data fidelity achieved between AIRI, uSARA, and R3D3, approaching that achieved by CLEAN. Specifically to R2D2 and R3D3, we observe structures with varying amplitudes in the residual dirty images, particularly at the inner core and around the hotspots regions. These are residual calibration errors, which the R2D2 model interestingly keeps out of its reconstruction.

### 5.2. Computational cost

All algorithms were run on Cirrus. During inference, they utilized 1 CPU core and/or 1 GPU (when applicable, see Table 1). R2D2 and R3D3, requiring a handful of iterations in their series, are able to deliver reconstructions in a matter of seconds. Both are at least five times faster than CLEAN, and orders of magnitudes faster than AIRI and uSARA (as shown in Table 1). Note that the computational times, reported for the highly iterative algorithms uSARA and AIRI, are indicative only, as they are sensitive to the allocated computing resources and the required levels of parallelization. In fact, when targeting orders of magnitude larger image dimensions, recent studies have shown a significantly narrower computational gap between CLEAN, AIRI, and uSARA (Dabbech et al. 2022; Wilber et al. 2023a,b). The conclusion remains that, based on the reported number of iterations, and thanks to a more efficient minor cycle than CLEAN, the R2D2 model presents a significant leap in computational efficiency over all the benchmarks, thus paving the way to real-time imaging.

## 6. CONCLUSIONS

We have introduced the R2D2 approach, a novel model-based DL algorithm, for high-resolution high-dynamic range RI. The R2D2 model encompasses a sequence of networks trained end-to-end within an iterative process, reminiscent of the matching pursuit algorithm, progressively identifying model components from the residual dirty images, in a similar fashion to CLEAN.

We have proposed two variants of the R2D2 model, each underpinned by a distinct DNN architecture. The first, dubbed R2D2 (for simplicity), relies on the stan-

dard U-Net architecture. The second, dubbed R3D3, relies on a novel unrolled architecture, inspired by the R2D2 model itself. Application of both R2D2 and R3D3 to highly-sensitive VLA observations of Cygnus A demonstrates an imaging precision that is (i) on par with the advanced RI algorithms uSARA and AIRI, achieved at only a fraction of their computational cost, and (ii) superior to CLEAN while being about five times faster. Our novel AI model thus paves the way for scalability to large-scale data, expected from next-generation radio telescopes.

Future research directions include: (i) investigating the robustness of the R2D2 model to accommodate more diverse imaging settings (such as varying data-weighting schemes, flexible super-resolution factors and image dimensions), and possibly revisiting the telescope-specific implementation in favor of an all-instrument-encompassing approach; and (ii) further improving its capability to deliver new regimes of precision and scalability, e.g., leveraging novel DNN architectures (including diffusion models, Ho et al. 2020) and training loss functions for more efficient and physics-informed training and reconstruction.

## 7. DATA AVAILABILITY

The imaged observations of Cygnus A were provided by the National Radio Astronomy Observatory (NRAO, Program code: 14B-336). The self-calibrated data can be shared upon request to R. A. Perley (NRAO). All Cygnus A reconstructions are available in FITS format from the research portal of Heriot-Watt University, with the digital object identifier [10.17861/99b62a21-204d-4a54-89da-07d7f74be741](https://doi.org/10.17861/99b62a21-204d-4a54-89da-07d7f74be741).

## ACKNOWLEDGMENTS

The authors warmly thank R. A. Perley (NRAO, USA) for providing the VLA observations of Cygnus A. The research of AA, AJ, AD and YW was supported by the UK Research and Innovation under the EPSRC grants EP/T028270/1 and EP/T028351/1, and the STFC grant ST/W000970/1. The research used Cirrus, a UK National Tier-2 HPC Service at EPCC funded by the University of Edinburgh and EPSRC (EP/P020267/1). The National Radio Astronomy Observatory is a facility of the National Science Foundation operated under cooperative agreement by Associated Universities, Inc.

*Facility:* The Very Large Array (VLA)

*Software:* WSClean (Offringa et al. 2014), Meqtrees (Noordam & Smirnov 2010),

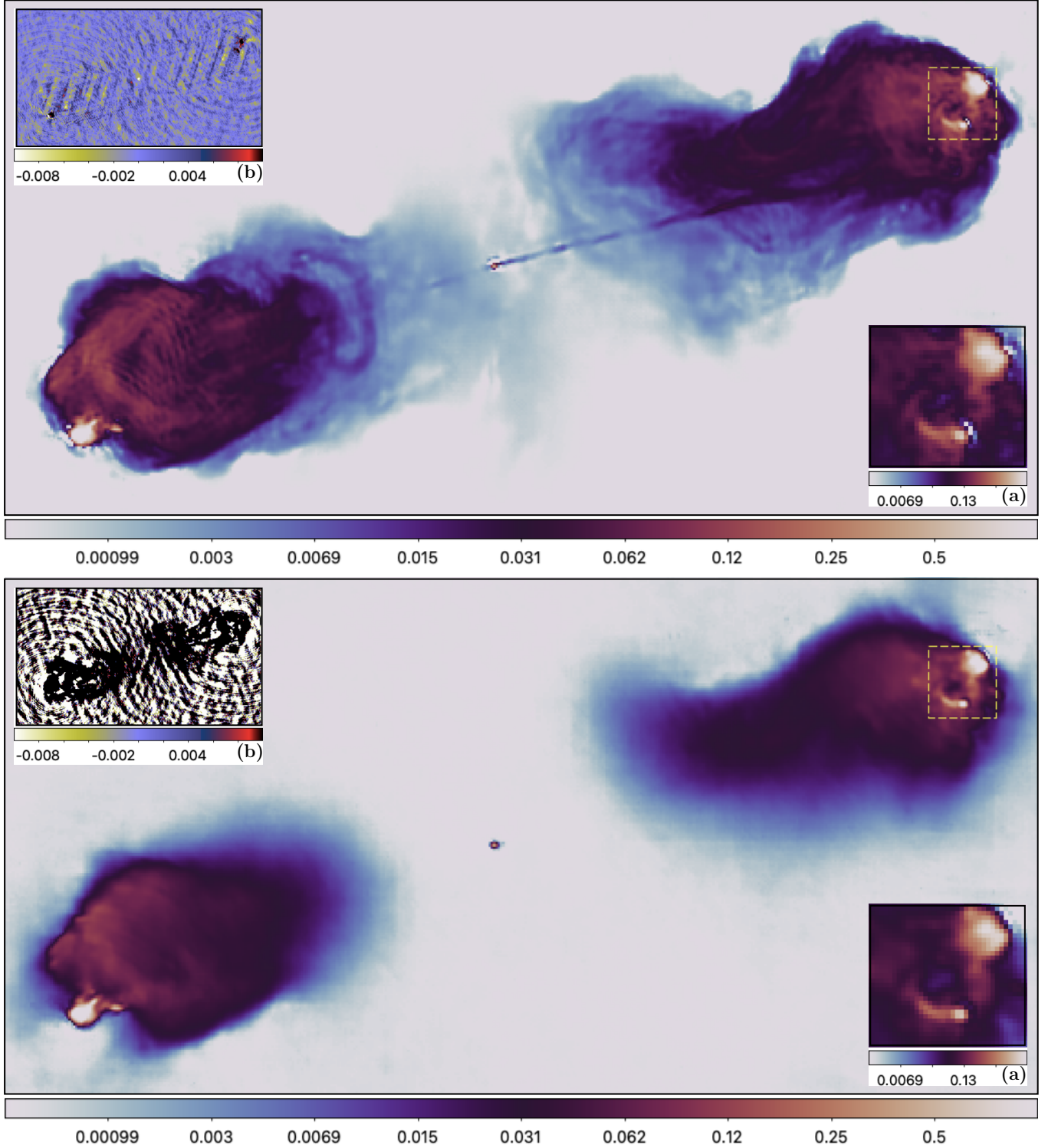


**Figure 2.** Cygnus A: reconstructions delivered by R2D2 (top) and U-Net (bottom, which also corresponds to the first term of the R2D2 series), both displayed in  $\log_{10}$  scale. These are overlaid by panels: (a) a zoom on the East hotspots in  $\log_{10}$  scale, and (b) the associated residual dirty image in linear scale. The images are available in FITS format in [Aghabiglou et al. \(2023\)](#).

## REFERENCES

Aghabiglou, A., Chu, C. S., Jackson, A., Dabbech, A., & Wiaux, Y. 2023, When R2D2 meets Cygnus A, doi: [10.17861/99b62a21-204d-4a54-89da-07d7f74be741](https://doi.org/10.17861/99b62a21-204d-4a54-89da-07d7f74be741)

Bhatnagar, S., & Cornwell, T. J. 2004, A&A, 426, 747

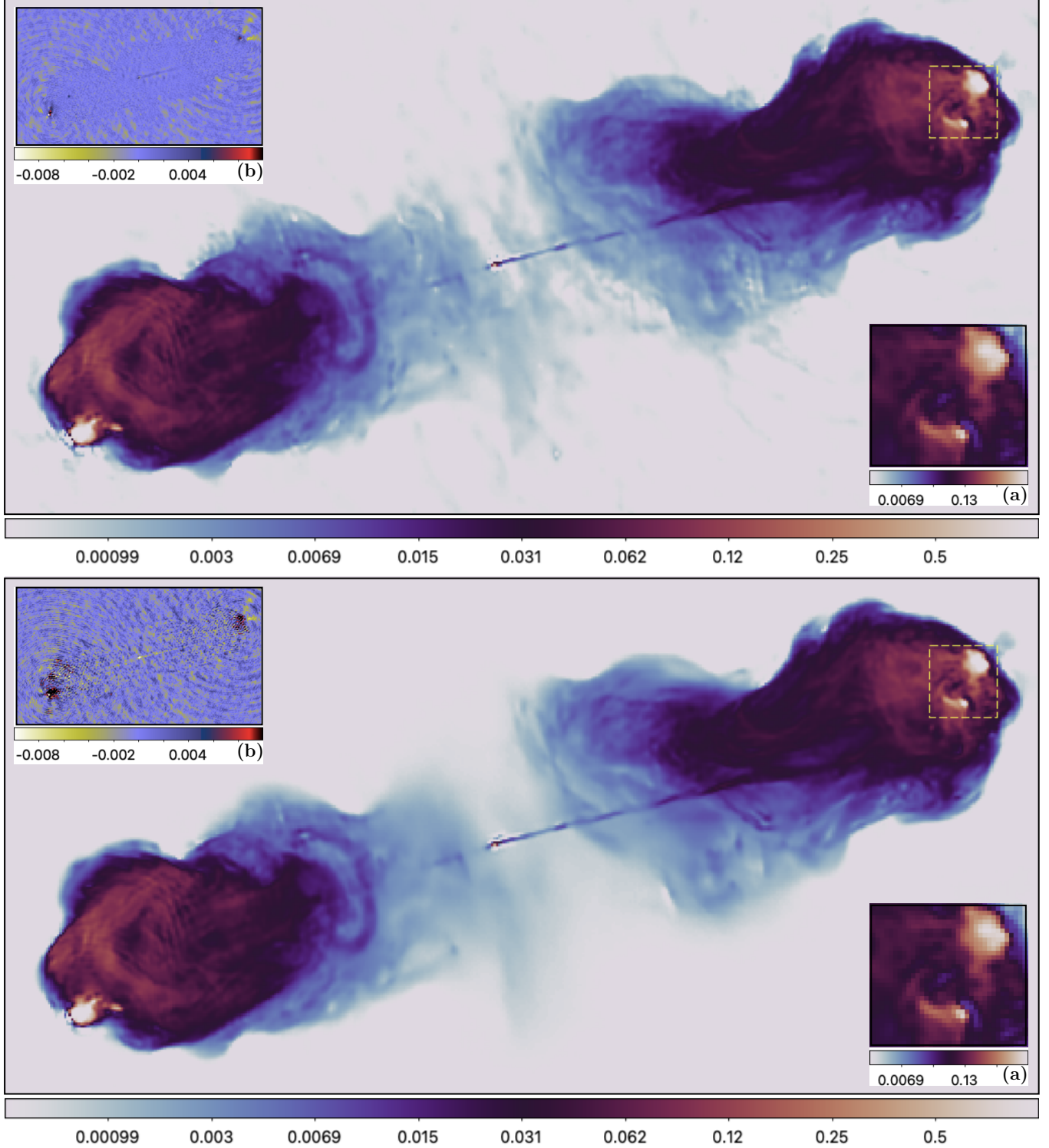


**Figure 3.** Cygnus A: reconstructions delivered by R3D3 (top) and R2D2-Net (bottom, which also corresponds to the first term of the R3D3 series), both displayed in  $\log_{10}$  scale. These are overlaid by panels: (a) a zoom on the East hotspots in  $\log_{10}$  scale, and (b) the associated residual dirty image in linear scale. The images are available in FITS format in [Aghabiglou et al. \(2023\)](#).

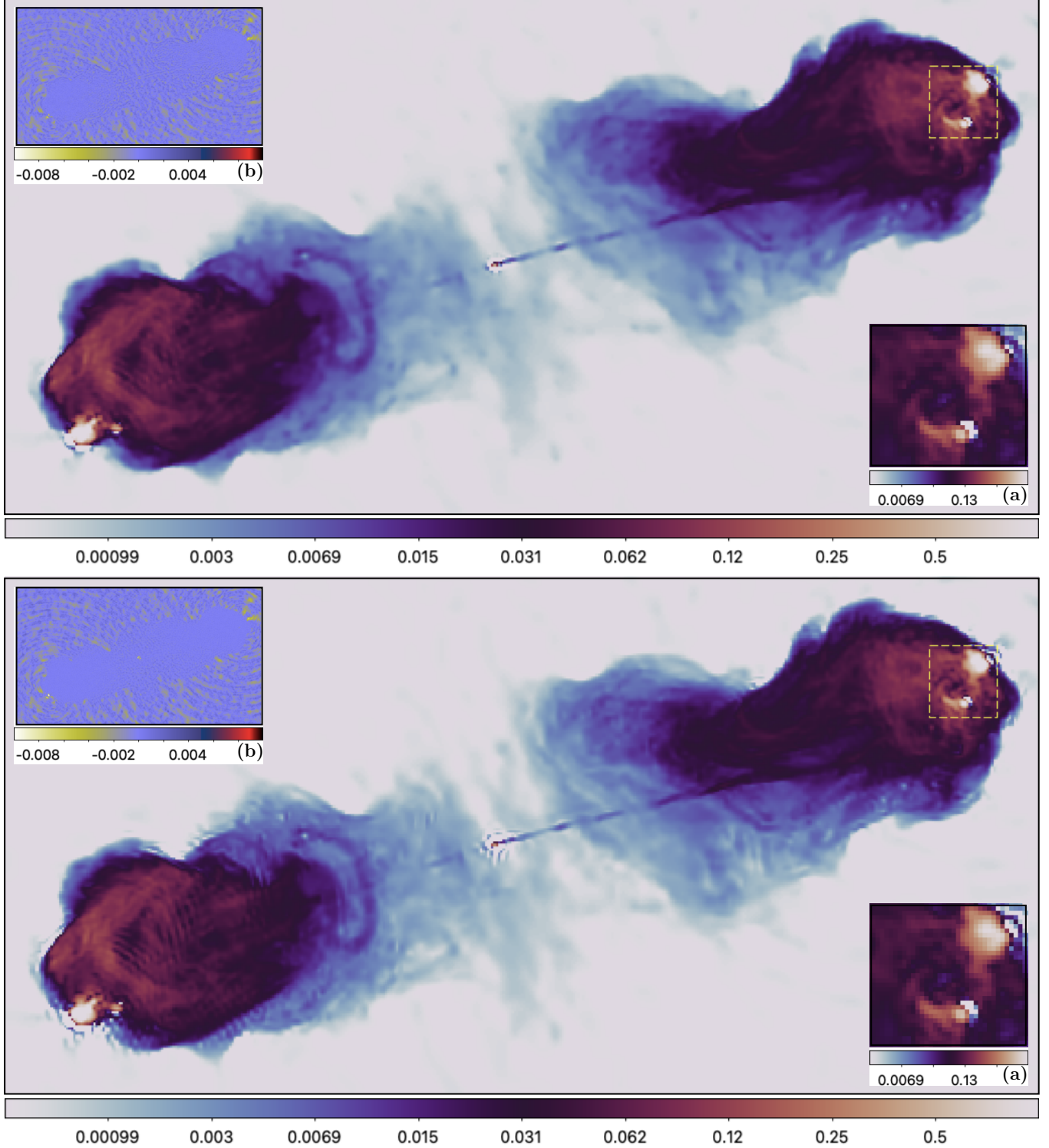


**Figure 4.** Cygnus A: reconstructions delivered by AIRI (top) and uSARA (bottom), both displayed in  $\log_{10}$  scale. These are overlaid by panels: (a) a zoom on the East hotspots in  $\log_{10}$  scale, and (b) the associated residual dirty image in linear scale. The images are available in FITS format in [Aghabiglou et al. \(2023\)](#).

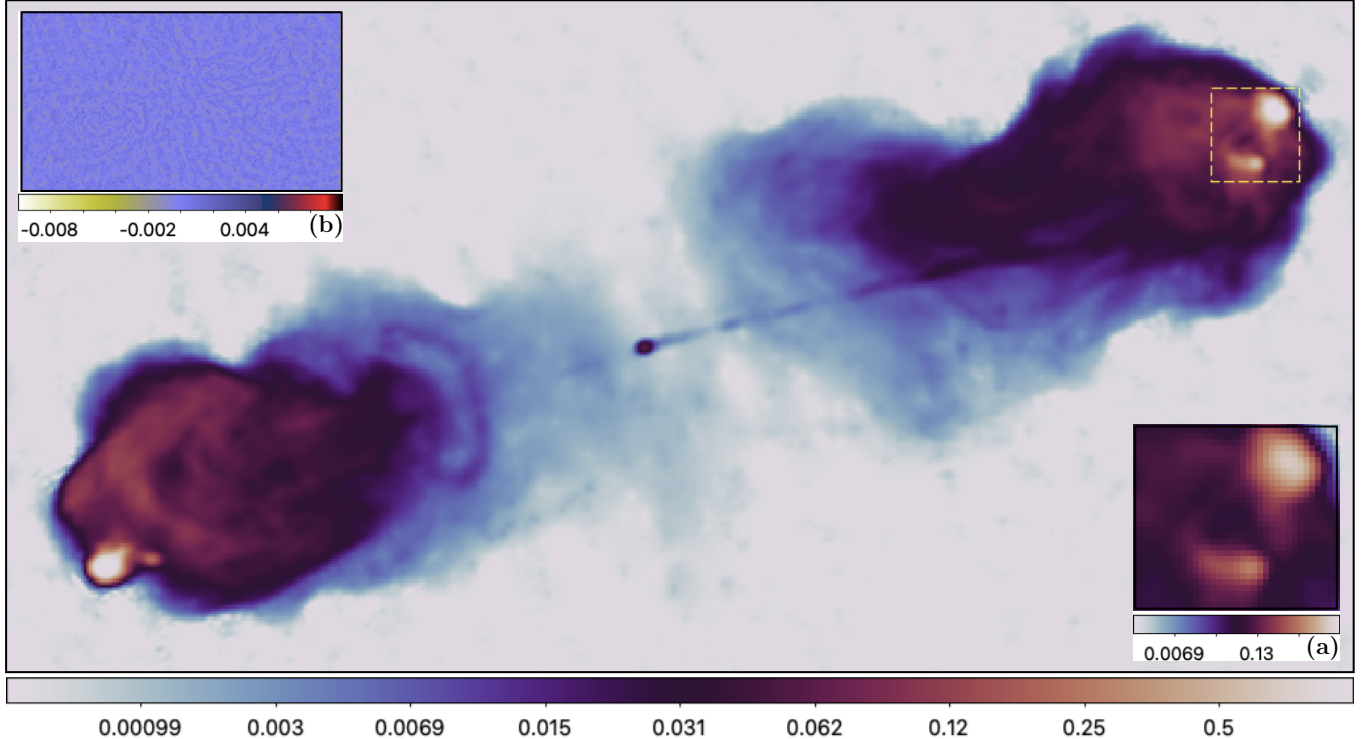


**Figure 5.** Cygnus A: CLEAN reconstruction, displayed in  $\log_{10}$  scale, and overlaid by panels: (a) a zoom on the East hotspots in  $\log_{10}$  scale, and (b) the associated residual dirty image in linear scale. Note that CLEAN reconstruction corresponds to the outcome of the convolution of the associated model image with the restoring beam, with the negative pixels set to zero for visualization purposes. The images are available in FITS format in [Aghabiglou et al. \(2023\)](#).

Dabbech, A., Ferrari, C., Mary, D., et al. 2015, *A&A*, 576, A7

Dabbech, A., Terris, M., Jackson, A., et al. 2022, *ApJL*, 939

Garsden, H., Girard, J., Starck, J.-L., et al. 2015, *A&A*, 575, A90

Gregor, K., & LeCun, Y. 2010, in *Proc. of ICML*, 399–406

Ho, J., Jain, A., & Abbeel, P. 2020, *Adv Neural Inf Process Syst*, 33, 6840

Högbom, J. 1974, *A&AS*, 15, 417

Kamilov, U. S., Bouman, C. A., Buzzard, G. T., & Wohlberg, B. 2023, *IEEE Signal Process. Mag.*, 40, 85

Li, F., Cornwell, T. J., & de Hoog, F. 2011, *A&A*, 528, A31

Monga, V., Li, Y., & Eldar, Y. C. 2021, *IEEE Signal Process. Mag.*, 38, 18

Noordam, J. E., & Smirnov, O. M. 2010, *A&A*, 524, A61

Offringa, A., McKinley, B., Hurley-Walker, N., et al. 2014, *MNRAS*, 444, 606

Repetti, A., & Wiaux, Y. 2020, in *Proc. of ICASSP 2020 IEEE*, 1434–1438

Ronneberger, O., Fischer, P., & Brox, T. 2015, in *Medical Image Computing and Computer-Assisted Intervention – MICCAI 2015*, 234–241

Schmidt, K., Geyer, F., Fröse, S., et al. 2022, *A&A*, 664, A134

Schwab, F. R. 1984, *AJ*, 89, 1076

Sebokolodi, M. L. L., Perley, R., Eilek, J., et al. 2020, *ApJ*, 903, 36

Smirnov, O. M. 2011, *A&A*, 527, A106

Terris, M., Dabbech, A., Tang, C., & Wiaux, Y. 2022, *Monthly Notices of the Royal Astronomical Society*, 518, 604

Wakker, B. P., & Schwarz, U. 1988, *A&A*, 200, 312

Wiaux, Y., Jacques, L., Puy, G., Scaife, A. M., & Vandergheynst, P. 2009, *MNRAS*, 395, 1733

Wilber, A. G., Dabbech, A., Jackson, A., & Wiaux, Y. 2023a, *MNRAS*, 522, 5558

Wilber, A. G., Dabbech, A., Terris, M., Jackson, A., & Wiaux, Y. 2023b, *MNRAS*, 522, 5576